PHYSICAL REVIEW APPLIED **9,** 034021 (2018)

Tunable Graphene Metasurface Reflectarray for Cloaking, Illusion, and Focusing

Sudipta Romen Biswas,[1] Cristian E. Gutiérrez,[2] Andrei Nemilentsau,[1] In-Ho Lee,[1]
Sang-Hyun Oh,[1] Phaedon Avouris,[3] and Tony Low[1,*]
[1]*Department of Electrical and Computer Engineering, University of Minnesota,*
Minneapolis, Minnesota 55455, USA
[2]*Department of Mathematics, Temple University, Philadelphia, Pennsylvania 19122, USA*
[3]*IBM T. J. Watson Research Center, Yorktown Heights, New York 10598, USA*

(Received 25 September 2017; revised manuscript received 11 December 2017; published 23 March 2018)

This paper is a contribution to the Physical Review Applied *collection in memory of Mildred S. Dresselhaus.*

We present a graphene-based metasurface that can be actively tuned between different regimes of operation, such as anomalous beam steering and focusing, cloaking, and illusion optics, by applying electrostatic gating without modifying the geometry of the metasurface. The metasurface is designed by placing graphene ribbons on a dielectric cavity resonator, where interplay between geometric plasmon resonances in the ribbons and Fabry-Perot resonances in the cavity is used to achieve a 2π phase shift. As a proof of concept, we demonstrate that the wave front of the field reflected from a triangular bump covered by the metasurface can be tuned by applying electric bias so as to resemble that of a bare plane and of a spherical object. Moreover, reflective focusing and the change of the reflection direction for the above mentioned cases are also shown.

DOI: 10.1103/PhysRevApplied.9.034021

I. INTRODUCTION

A gradient metasurface is a planar arrangement of subwavelength scatterers of different shapes and sizes designed to structure wave fronts of reflected or transmitted optical beams by means of spatially varying the optical response [1–5]. Light interaction with the metasurfaces defies the conventional laws of geometrical optics, such as Snell's law or the law of reflection, and reveals a variety of nontrivial physical effects useful for practical applications. Specifically, efficient beam steering of the incident light in reflection and/or transmission modes was reported for metasurfaces operating in both narrow [6,7] and broad [8–11] frequency ranges. Moreover, pronounced polarization dependence of the steering directions and/or amplitudes of beams deflected by metasurfaces has been demonstrated [12–18], thus paving the way for the creation of ultrathin optical polarizers and quarter- and half-wave plates [19–21]. A great deal of attention has also been devoted to developing viable alternatives to conventional focusing devices in transmission (lenses) [7,22–25] and reflection (parabolic reflectors) [26–31] geometries. In fact, reflectarrays allow for the implementation of a parabolic phase gradient along a planar surface, thus avoiding the technologically complicated process of creating parabolic surfaces for reflected light.

Recently, it was learned that metasurfaces can replace transformation optics [32–34] when it comes to implementing efficient cloaking devices. The essence of optical cloaking is to surround the object to be hidden by a material with carefully designed spatially varying dielectric permittivity (optical cloak) so that the far-field radiation pattern of the object-cloak system is as close as possible to that of empty space. The efficient hiding of 2D and 3D bumps by metasurface carpet cloaks has been reported [35–40]. The advantage of metasurface-based cloaking is that control of the polarization, phase, and amplitude of the wave reflected by a cloaked object can be achieved [41] without modifying all of the components of permittivity and permeability tensors, which is required when using the transformation optics approach.

The operational characteristics (angle of beam steering, focal distance, angular efficiency, losses, etc.) of optical devices based on metasurfaces designed using conventional dielectric or metal materials is typically predefined by the metasurface geometry and cannot be changed on the fly during the device operation. This might be a significant limitation when tuning of the device characteristics is essential for device operation, particularly with the tunable steering angle for optical switches. Attempts to overcome this limitation using gate-tunable conducting oxides [42], temperature-tunable nematic liquid crystals [43], or strain-tunable elastic polymers [44] as metasurface building blocks have been reported. Graphene plasmonic resonators [45–51] provide a viable alternative [52–55] to design of

---

[*] tlow@umn.edu

an active metasurface that can be tuned by applying gate voltage. Dynamic tuning of Fermi energy in graphene plasmonic structures has been reported for optical switching [56] and infrared beam steering via acoustic modulation [57]. Active tuning of the steering angle using graphene-based metasurfaces operating in the reflection regime has been reported [54,58].

The gradient metasurfaces are typically designed to perform a particular specialized task, such as tuning, focusing, or cloaking. In this paper, we demonstrate that it is possible to design a versatile active metasurface using gate-tunable graphene ribbons [59,60] on an arbitrary substrate surface which is capable of performing each of the abovementioned specialized tasks depending on the electric bias profile across the surface of the metasurface, i.e., without changing the metasurface geometry. Specifically, we demonstrate that far-field distribution of the electric field of the wave reflected from a bump covered by such a metasurface can resemble either that of bare plane (the cloaking case) or that of an object of a different shape (illusion), depending on the applied bias. In addition, we show that such wave-front engineering—as anomalous reflection and focusing—can also be achieved in conjunction with cloaking and illusion.

In what follows, we discuss general metasurface design strategy in Sec. II, followed by theoretical and simulation results for the abovementioned functionalities in Secs. III–V. We end with some general discussions on the experimental realization and performance issues of the device in Sec. VI.

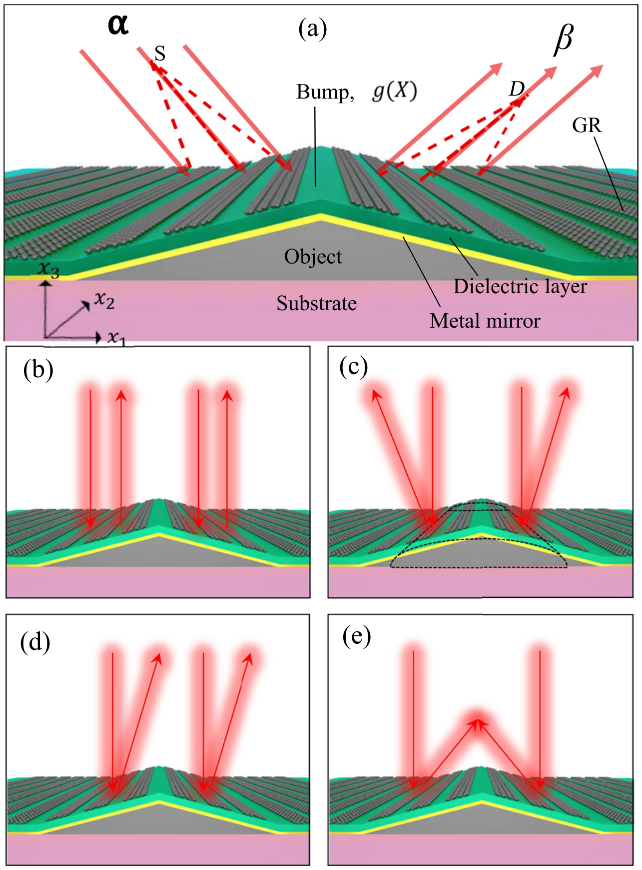

FIG. 1. Illustration of the metasurface design and applications. (a) Structure of the graphene ribbon (GR) array metasurface covering a nonplanar surface. $\boldsymbol{\alpha}$ and $\boldsymbol{\beta}$ are the directions of the incident and reflected rays. (b)–(e) Depictions of different reflection jobs discussed in the work. They are (b) cloaking with specular reflection, (c) illusion optics, (d) cloaking with anomalous reflection, and (e) reflective focusing.

II. DESIGN OF THE METASURFACE

Figure 1(a) shows a schematic of the graphene-based metasurface device. In general, the metasurface can be implemented on a nonplanarized surface. At the desired frequencies, midinfrared light incident on the metasurface can be reflected in a nontrivial fashion to achieve various functionalities. For example, the light can be reflected as if the surface is planar [see Fig. 1(b)] or disguised as a different surface morphology [see Fig. 1(c)]. The former is often referred to in the literature as cloaking [61,62], the latter as illusion optics [63]. The light can also be anomalously reflected to far field as a plane wave in a predetermined direction [see Fig. 1(d)], or onto a focal point at the near field [see Fig. 1(e)], all achieved on a nonplanar substrate.

The general implementation of these various reflection modes can be achieved with the appropriate phase discontinuities, ϕ, at the graphene metasurface. The phase discontinuity for any arbitrary reflection beam wave front can be derived from ray-optics arguments. Let us consider a general surface in 3D space, with coordinates of a point P on the surface defined as

$$P = (u_1, u_2, u_3), \tag{1}$$

where $u_1 = x_1,\ u_2 = x_2,\ u_3 = g(X),\ X = (x_1, x_2)$ [see Fig. 1(a)]. The normal to the metasurface, $\boldsymbol{\nu}(P)$, is

$$\boldsymbol{\nu}(P) = \frac{(-\boldsymbol{\nabla} g(X), 1)}{\sqrt{1 + |\boldsymbol{\nabla} g(X)|^2}}. \tag{2}$$

Suppose, $\boldsymbol{\alpha}(P)$ and $\boldsymbol{\beta}(P)$ are unit direction vectors for incident and reflected waves. Absent any phase discontinuity along the surface, we can write the vector form of the conventional Snell's law as [64]

$$\boldsymbol{\alpha}(P) \times \boldsymbol{\nu}(P) = \boldsymbol{\beta}(P) \times \boldsymbol{\nu}(P), \tag{3}$$

which is equivalent to $[\boldsymbol{\alpha}(P) - \boldsymbol{\beta}(P)] \times \boldsymbol{\nu}(P) = 0$; i.e., $\boldsymbol{\alpha}(P) - \boldsymbol{\beta}(P)$ is parallel to $\boldsymbol{\nu}(P)$. Therefore, we can write [64,65]

$$\boldsymbol{\alpha}(P) - \boldsymbol{\beta}(P) = \lambda \boldsymbol{\nu}(P),$$

where λ is a scalar factor, $\lambda \in \mathbb{R}$. When we have a phase discontinuity, given by a function ϕ, defined in the neighborhood of the surface, the generalized law of reflection in vector form [65] is given by (Appendix A)

$$\boldsymbol{\alpha}(P) - \boldsymbol{\beta}(P) = \frac{\nabla\phi(P)}{k_0} + \lambda\boldsymbol{\nu}(P), \tag{4}$$

where k_0 is the free-space wave number. Based on the desired operation, one would stipulate the required scattering beams $\boldsymbol{\alpha}$ and $\boldsymbol{\beta}$, and, starting from Eq. (4), we can calculate the respective phase profiles ϕ. We defer these calculations to Secs. III–V.

In practice, design of a phase-control metasurface involves two steps [3]. First, a phase profile or phase mask for the desired wave-front modification is calculated, and then individual pixels of the phase profile, which locally tailor the phase of the impinging wave, are designed. The scattering phase is achieved with graphene ribbons [45–48,50], whose plasmon resonance is tunable with doping or width. In this work, we fix the ribbon widths and vary the doping to achieve the desired phase, ϕ.

Figure 1(a) provides an illustration of the graphene-ribbon-based metasurface on a dielectric layer. There is a metal mirror below the dielectric layer separated at quarter-wavelength distance from the graphene arrays. This quarter-wavelength condition maximizes the field at the graphene surface, hence enhancing light-matter interactions [54]. To have total control over the wave front, the phase shift along the metasurface needs to encompass the full 2π range. A graphene ribbon, with its Lorentzian-like response, provides a phase shift of only π. The interference between the graphene resonator and the Fabry-Perot cavity provides the extra phase shift to make the total range of phase variation very close to 2π [54]. From the phase profile function, $\phi(P)$, which we derive in Secs. III–V, we will be able to assign the required phase to each respective ribbon.

In this work, graphene conductivity is described with the finite-temperature Drude formula which accounts for the intraband optical processes,

$$\sigma(E_F) = \frac{2e^2}{\pi\hbar^2} k_B T \log\left[2\cosh\left(\frac{E_F}{2k_B T}\right)\right] \frac{i}{\omega + i\tau^{-1}}. \tag{5}$$

E_F is the Fermi level of the ribbon, which is chosen according to the desired scattering phase, ω is the angular frequency taken to be equal to a free-space wavelength of 22 μm, τ is the graphene relaxation time, e is the electronic charge, and $T = 300$ K is the temperature. While choosing the value for relaxation time, the fact that plasmon damping increases due to the interaction with optical phonons from graphene and the substrate should be considered [59]. In this work, we assume a free-space wavelength of 22 μm, which is significantly lower than the optical phonon energy (about 0.2 eV) in graphene. Moreover, we assume a substrate that does not have surface optical phonons at the operating frequency, so a choice of relaxation time > 0.1 ps to ensure the availability of a 2π shift (see Appendix B) is justified. For example, CaF_2 is transparent in the midinfrared frequency region. We use a value of $\tau = 0.6$ ps [59]. For the dielectric layer, we assume a lossless refractive index of $n = 1.4$, with a thickness of 3.93 μm corresponding to the quarter-wavelength condition.

Simulations are performed using the Maxwell equation solver COMSOL Multiphysics [66] rf module. We model each graphene ribbon in terms of its 2D current density. To do so, we need to translate the spatial phase profile into the corresponding conductivity profile. First, we define the position of each ribbon by the coordinates of its center. Then, using the phase profiles ϕ derived in Secs. III–V, we get the discrete phase values for the ribbons. Using these phase values, we can determine the corresponding Fermi energy (E_F) for the individual ribbons. Then we get the required conductivity by putting the E_F values in the Drude equation [Eq. (5)]. Finally, in COMSOL, we use this spatial conductivity profile, defined for each ribbon, as the conductivity of the surface current densities. A fixed ribbon width of 500 nm and an inter-ribbon distance of 750 nm are used. E_F is varied between 0.15 and 0.8 eV. Perfectly matched layer conditions are used at the simulation domain boundaries, and the metal reflector is modeled with a perfect electric conductor.

III. CLOAKING: SPECULAR AND ANOMALOUS REFLECTION

In this section, we derive the phase function, $\phi(P)$, required for cloaking with specular or anomalous reflected beams. We assume that the metasurface is parametrized by Eqs. (1) and (2). Following Eq. (4), we seek ϕ such that the metasurface reflects all incident rays with direction $\boldsymbol{\alpha}$ into rays with direction $\boldsymbol{\beta}$, where $\boldsymbol{\alpha}$ and $\boldsymbol{\beta}$ are constant with respect to P. Taking a double cross-product of Eq. (4) with $\boldsymbol{\nu}(P)$ yields

$$\begin{aligned} 0 &= \boldsymbol{\nu} \times [(\boldsymbol{\alpha} - \boldsymbol{\beta} - \nabla\phi/k_0) \times \boldsymbol{\nu}] \\ &= (\boldsymbol{\alpha} - \boldsymbol{\beta} - \nabla\phi/k_0) - [\boldsymbol{\nu} \cdot (\boldsymbol{\alpha} - \boldsymbol{\beta} - \nabla\phi/k_0)]\boldsymbol{\nu}. \end{aligned} \tag{6}$$

We seek ϕ such that $\nabla\phi(P) = (\phi_{u_1}(P), \phi_{u_2}(P), \phi_{u_3}(P))$ is tangential to the surface, i.e., $\boldsymbol{\nu} \cdot \nabla\phi = 0$. Here and in rest of the paper, the notation $\phi_{u_i}(P)$ indicates the derivative of $\phi(P)$ with respect to u_i. Therefore, from Eqs. (2) and (6), we obtain

$$\nabla\phi(P) = k_0\{\boldsymbol{\alpha} - \boldsymbol{\beta} - \delta(-\nabla g(X), 1)\}, \tag{7}$$

where

$$\delta = \left(\frac{(\boldsymbol{\alpha} - \boldsymbol{\beta}) \cdot (-\nabla g(X), 1)}{1 + |\nabla g(X)|^2}\right). \tag{8}$$

Equation (7) is a system of three differential equations for an unknown phase function, $\phi(P)$, written in vector form (see Appendix C for the coordinate form), which can be reduced to two equations by taking into account that $\phi(P)$ is, in fact, a function of two variables, x_1 and x_2 [see Eq. (1)]. Using the chain rule, we obtain

$$\frac{\partial\phi}{\partial x_i}=\frac{\partial\phi}{\partial u_i}+\frac{\partial\phi}{\partial u_3}\frac{\partial u_3}{\partial x_i}=k_0[\alpha_i-\beta_i+(\alpha_3-\beta_3)g_{x_i}(X)], \tag{9}$$

where $i = 1$ and 2, $g_{x_i}(X) = \partial g(X)/\partial x_i$, and $\partial\phi/\partial u_i$ are defined by Eq. (7). Integrating, we obtain the phase

$$\begin{aligned}\phi[X,g(X)] = k_0[(\alpha_1-\beta_1)x_1+(\alpha_2-\beta_2)x_2\\ +(\alpha_3-\beta_3)g(X)]+C,\end{aligned} \tag{10}$$

with C being an arbitrary constant. For a 2D geometry, i.e., where the equations are independent of x_2, the last equation can be written as

$$\phi(x_1) = k_0[(\alpha_1-\beta_1)x_1+(\alpha_3-\beta_3)g(x_1)]+C. \tag{11}$$

In terms of the incident angle θ_i and the reflection angle θ_r, we have $\boldsymbol{\alpha} = (-\sin\theta_i, -\cos\theta_i)$, $\boldsymbol{\beta} = (-\sin\theta_r, \cos\theta_r)$. Therefore, in terms of θ_i and θ_r, Eq. (11) becomes

$$\phi(x_1) = k_0[(\sin\theta_r-\sin\theta_i)x_1-(\cos\theta_r+\cos\theta_i)g(x_1)]+C. \tag{12}$$

This is the general phase equation for cloaking. When $\theta_r = \theta_i$, we have the phase for cloaking with specular reflection.

Figure 2 shows simulation results for the specular cloaking case. We have a triangular bump with a base length of 100 μm and a height of 40 μm as the object to be cloaked. Results are shown for a normal incidence of light. Figures 2(a) and 2(b) show scattered-field (magnetic field H_y) plots for the bare bump and the bare ground plane, respectively. Next, the bump is cloaked by the metasurface designed with the abovementioned ϕ value, and the scattered-field plot is shown in Fig. 2(c). The accompanying angle-resolved far-field intensity plots are shown in log scale in Fig. 2(d). As we can see, within the angular window of ±40°, the angle-resolved intensity spectrum for the cloaked bump and bare ground plane far field match very well. The presence of sidelobes in the far field for the bare ground plane can be attributed to the finiteness of the simulation domain. If we increase the size of the simulation domain, both the mainlobes and the sidelobes become narrower and, ideally, with an infinitely large simulation domain, we can expect only one narrow mainlobe.

In similar fashion, we can also implement an extended version of the cloak, but with a nonspecular reflection angle. Figure 3(a) demonstrates such an implementation, designed with a 30° angle of reflection off normal. In Figs. 3(a) and 3(b), the scattered fields are shown for a normal and a 45° angle of incidence, respectively. The white and black arrows show the incident and reflected wave directions. There are some distortions in the wave fronts, predominantly due to specular reflections from the ground plane. In addition, we can also notice specular reflection on the right side of the bump. As we can see, the main beam is scattered at 30° off normal per the design,

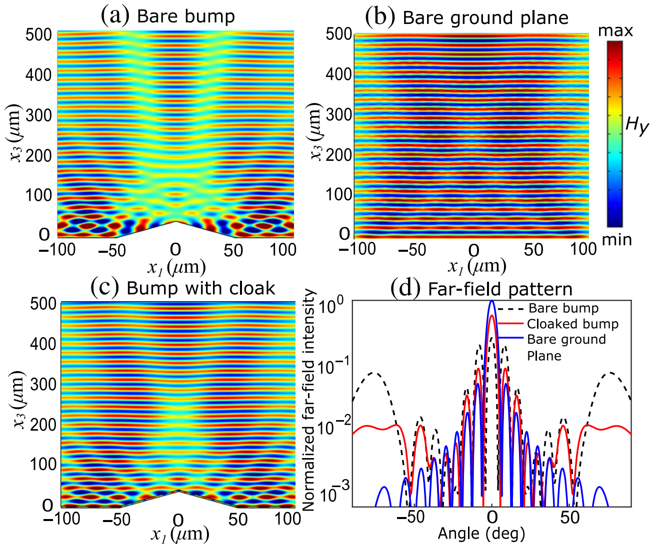

FIG. 2. Simulation results for cloaking with specular reflection. The cloaked object is a triangle-shaped bump. (a)–(c) Scattered-field plots for the bare bump, the ground plane, and the cloaked bump, respectively. (d) Corresponding far-field plots.

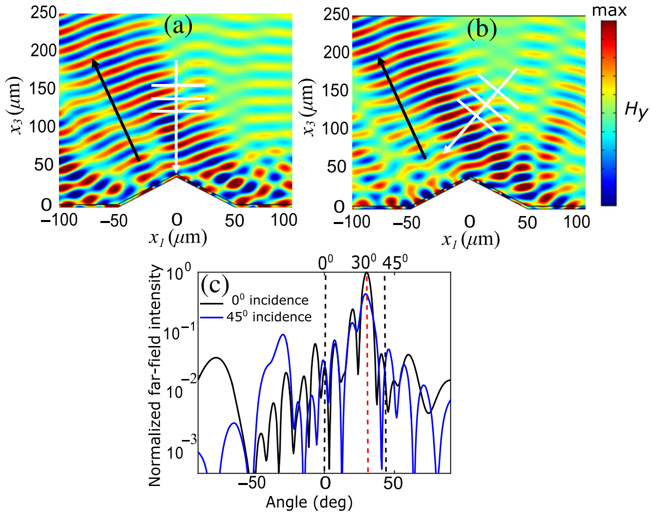

FIG. 3. Simulation results for cloaking with anomalous reflection. (a),(b) Scattered-field plots for a normal and a 45° incidence, respectively. For both cases, the angle of reflection is designed to be 30°. (c) The corresponding far-field plots.

while the power flow in specular directions (0° and 45°) is more than an order of magnitude smaller.

IV. ILLUSION OPTICS

Suppose that a surface Γ' in 3D space is parametrized by a function $(X, f(X))$, and no phase discontinuity is given on Γ'. The reflection of the rays by such a surface is governed by the standard Snell's law of reflection,

$$\boldsymbol{\beta}(P') = \boldsymbol{\alpha} - 2[\boldsymbol{\alpha}\cdot\boldsymbol{\eta}(P')]\boldsymbol{\eta}(P'), \tag{13}$$

where $P' = (X, f(X))$ is a point on Γ', $\boldsymbol{\alpha}$ and $\boldsymbol{\beta}(P')$ are the unit direction vectors for the incident and reflected waves, and $\boldsymbol{\eta}(P') = [(-\boldsymbol{\nabla} f(X), 1)/\sqrt{1+|\boldsymbol{\nabla} f(X)|^2}]$ is the unit normal.

We consider another metasurface, Γ, parametrized by Eqs. (1) and (2) and derive a phase discontinuity, $\phi(P)$, such that the metasurface (Γ, ϕ) does the same reflecting job as the surface Γ'. That is, at each point P, the incident ray with unit direction $\boldsymbol{\alpha}$ is reflected into the ray with unit direction $\boldsymbol{\beta}(P')$ given in Eq. (13). From Eq. (4), we then seek ϕ such that

$$\boldsymbol{\alpha} - \boldsymbol{\beta}(P') - \frac{\boldsymbol{\nabla}\phi(P)}{k_0} = \lambda\boldsymbol{\nu}(P). \tag{14}$$

As in Sec. III, making a double cross-product of this equation with $\boldsymbol{\nu}$ and assuming that $\boldsymbol{\nabla}\phi\cdot\boldsymbol{\nu} = \mathbf{0}$ yields

$$\begin{aligned}\frac{\boldsymbol{\nabla}\phi(P)}{k_0} &= \boldsymbol{\alpha} - \boldsymbol{\beta}(P') - \{[\boldsymbol{\alpha} - \boldsymbol{\beta}(P')]\cdot\boldsymbol{\nu}(P)\}\boldsymbol{\nu}(P)\\ &= 2[\boldsymbol{\alpha}\cdot\boldsymbol{\eta}(P')]\{\boldsymbol{\eta}(P') - [\boldsymbol{\eta}(P')\cdot\boldsymbol{\nu}(P)]\boldsymbol{\nu}(P)\},\end{aligned} \tag{15}$$

where we use Eq. (13) to obtain the second line. Equation (15) is a vector form of a system of three differential equations (see Appendix C for coordinate form) which, once again, can be simplified using the chain rule,

$$\begin{aligned}\frac{\partial\phi}{\partial x_i} &= \frac{\partial\phi}{\partial u_i} + \frac{\partial\phi}{\partial u_3}\frac{\partial u_3}{\partial x_i}\\ &= 2k_0[\boldsymbol{\alpha}\cdot\boldsymbol{\eta}(P')]\frac{g_{x_1}(X) - f_{x_1}(X)}{\sqrt{1+|\boldsymbol{\nabla} f(X)|^2}} \coloneqq A_i(X),\end{aligned} \tag{16}$$

where $i = 1$ and 2. Integrating a system of two differential equations, Eq. (16), we obtain (see Appendix D for details)

$$\phi(X, g(X)) = \int_a^{x_1} A_1(s, x_2)ds + \int_b^{x_2} A_2(a, t)dt + C. \tag{17}$$

For the case where the configuration is independent of x_2, Eq. (17) can be simplified to

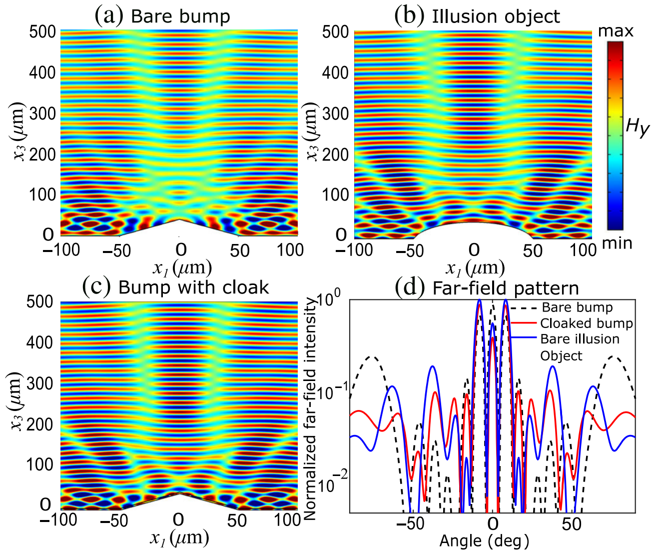

FIG. 4. Simulation results for illusion optics. The cloaked object is a triangle-shaped bump, and the illusion object is a circular segment. (a)–(c) show the scattered-field plots for the bare bump, the bare illusion object, and the cloaked bump, respectively. (d) The corresponding far-field plots.

$$\phi(x_1) = 2k_0\int_a^{x_1}\frac{[-\alpha_1 f'(s) + \alpha_3][g'(s) - f'(s)]}{1 + f'(s)^2}ds + C, \tag{18}$$

which gives the phase required to be applied along a surface $g(x_1)$ to mimic the reflection pattern of another surface, $f(x_1)$.

Figure 4 shows the simulation results implementing the abovementioned ϕ for illusion optics. We have the same triangular bump as the object to be cloaked (i.e., Γ'), and a circular segment with chord length of 100 μm and height of 40 μm as the desired illusion object (i.e., Γ). Figures 4(a) and 4(b) show scattered-field plots for the bare bump and the illusion object, respectively. When the triangular bump is cloaked by the designed metasurface, the scattering pattern becomes similar to that of the illusion object, which would make the triangular bump appear to be a circular bump to an external observer. The field plot for the cloaked object is shown in Fig. 4(c). Angle-resolved far-field intensity plots are shown in Fig. 4(d) for a comparison of these three cases. There is good agreement between the cloaked bump and the illusion object in the far field, especially within the angular window of ±50°.

V. REFLECTIVE FOCUSING

In this section, we consider focusing a plane wave onto a point $D(d_1, d_2, d_3)$ using a metasurface parametrized by Eqs. (1) and (2) [see Fig. 1(e)]. Assuming that $\boldsymbol{\alpha}$ is the constant unit incident vector, we rewrite Eq. (4) as

$$\boldsymbol{\alpha} - \frac{D-P}{|D-P|} - \frac{\boldsymbol{\nabla}\phi(P)}{k_0} = \lambda \boldsymbol{\nu}(P),$$

where $\phi(P)$ is the phase discontinuity along the metasurface and $(D-P)/|D-P|$ is the unit reflected vector. Making the double cross-product with $\boldsymbol{\nu}$ yields

$$\frac{\boldsymbol{\nabla}\phi(P)}{k_0} = \boldsymbol{\alpha} - \frac{D-P}{|D-P|} - \left[\left(\boldsymbol{\alpha} - \frac{D-P}{|D-P|}\right)\cdot\boldsymbol{\nu}\right]\boldsymbol{\nu}. \qquad (19)$$

The system of differential equations (19) (see Appendix C for the coordinate form) can be simplified by calculating derivatives of the phase function, $\phi(P)$, with respect to x_1 and x_2, using the chain rule [see Eq. (9)],

$$\begin{aligned}\frac{\partial\phi}{\partial x_i} &= k_0\left[\alpha_i - \frac{d_i - x_i}{|D-P|} + \left(\alpha_3 - \frac{d_3 - g(X)}{|D-P|}\right)g_{x_i}(X)\right]\\ &= k_0\left(\frac{\partial}{\partial x_i}|D-P| + \frac{\partial}{\partial x_i}[\alpha_i x_i + \alpha_3 g(X)]\right),\end{aligned}$$

with $i = 1$ and 2. Therefore, we obtain the phase

$$\phi(X, g(X)) = k_0[|D-P| + \boldsymbol{\alpha}\cdot(X, g(X))] + C.$$

For a 2D geometry independent of x_2, $D = (x_d, z_d)$, and $\boldsymbol{\alpha} = (-\sin\theta_i, -\cos\theta_i)$, the phase equation reduces to

$$\begin{aligned}\phi(x_1) = k_0\Big\{&\sqrt{(x_1 - x_d)^2 + [g(x_1) - z_d]^2} - x_1\sin\theta_i\\ &- g(x_1)\cos\theta_i\Big\} + C. \qquad (20)\end{aligned}$$

In a similar way, we can demonstrate (see Appendix E) that the phase discontinuity

$$\begin{aligned}\phi(x_1) = k_0\Big\{&\sqrt{(x_1 - x_s)^2 + [g(x_1) - z_s]^2}\\ &+ \sqrt{(x_1 - x_d)^2 + [g(x_1) - z_d]^2}\Big\} + C \qquad (21)\end{aligned}$$

should be imposed on the metasurface for focusing rays radiated by a point source located at $S = (x_s, z_s)$.

Simulation results for reflective focusing of incident parallel beams (the plane wave) and the point dipole source are shown in Fig. 5. In the scattered-field intensity plots of Figs. 5(a), 5(b), and 5(c), we have incident parallel beams focused on a point at a distance of 150 μm from the base of the triangular bump (i.e., the ground plane). First, we consider normal incidence. Figures 5(a) and 5(b) show the simulation results for normal incidence. Last, we consider oblique incidence with a 30° angle in Fig. 5(c). The direction of incidence is indicated by white arrows and the position of the focusing point is indicated with an ×. Flat gradient metasurfaces allow high-NA diffraction-limited focusing without spherical abberation [2,7]. The size of the focal spot in Figs. 5(a)–5(c) is comparable to the free-space wavelength of 22 μm.

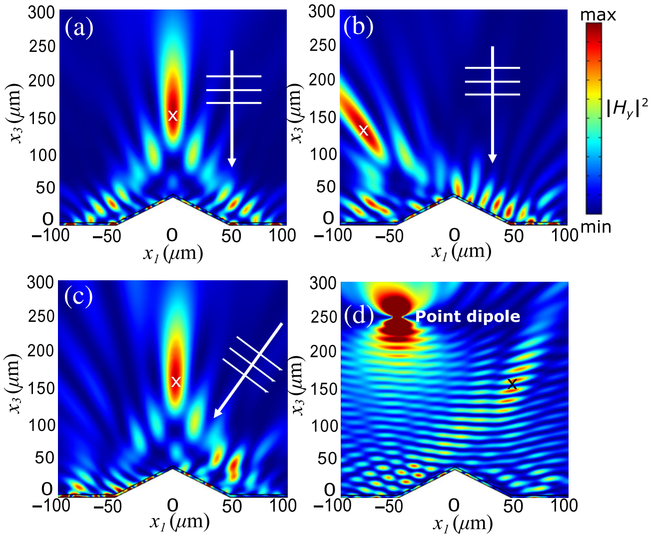

FIG. 5. Simulation results for reflective focusing off of an arbitrary surface. (a)–(c) Field intensity plots for focusing of an incident plane wave to a focal distance of 150 μm from the ground plane. (a),(b) show normal incidence while (c) shows the result for 30° incidence. In (a) and (c), the focal point is located 150 μm away in the normal direction, while, in (b), the focal point is at an angle of 30°. (d) Focusing of a point dipole source.

In Fig. 5(d), an example shows the focusing of a point source. The source is at $(-50, 250)$ μm and the focusing point is at $(50, 150)$ μm. The point source is modeled by a electric point dipole in COMSOL, with its dipole moment oriented along the x_1 direction. As there is no straightforward way to use a point source for scattered-field calculation in COMSOL, we simulate for the total field instead, with a point dipole acting as a point source. The plotted quantity in Fig. 5(d) is the total field intensity; i.e., both the incident and reflected fields are present. We can see a higher intensity of field around the designed focus point, indicating the focusing effect.

VI. DISCUSSION AND CONCLUSION

In conclusion, we demonstrate in this paper the versatility of a graphene-based metasurface that is capable of active switching between regimes of operation—such as anomalous beam steering, focusing, cloaking, and illusion optics—simply by changing the electric bias applied to the graphene constituents of the metasurface without changing the metasurface geometry. These various functionalities are usually available in a disparate manner in the existing literature, and we show in this work that they can be described within a general framework for an arbitrary surface morphology. The proposed approach, particularly in the context of a graphene metasurface, makes perfect sense since graphene can be electrically tunable to achieve arbitrary phase function and it conforms to any surface morphology. As an example, we consider in the paper a triangular bump covered by a graphene metasurface, made from graphene ribbons on the dielectric resonator, and demonstrate that, by applying an electric bias, the wave front of the wave reflected by the bump can be tuned to match that of the bare plane (cloaking) or the hemisphere (illusion optics). Moreover, the possibility of anomalous steering and focusing of the wave reflected by a graphene-metasurface-covered bump is shown. The slight distortion of the metasurface far-field radiation pattern from that of the bare plane or hemisphere can be attributed to the specular reflection from the parts of the metasurface not covered by graphene ribbons, as well as to the fact that the reflectivity of the graphene ribbon depends on the applied electric bias. Finite-size effects also show up in the field profile due to the finiteness of the simulation domain, the discretization of the metasurface, and the contribution from the apex of the triangle [37,67]. We expect that, by optimizing the metasurface geometry, these distortions can be reduced.

The device configuration considered here can be fabricated with conventional film deposition and nanopatterning technologies. The transfer of graphene [68,69] onto the bump structure and its patterning by electron-beam lithography would be straightforward, as demonstrated elsewhere [70,71]. Nevertheless, there are a few issues that need to be addressed in terms of practical implementation. First, we should select a proper material for an optical spacer which is transparent over the concerned frequency range and compatible with conventional thin-film-deposition technologies. In addition, it is important to have limited roughness on the film surface for the graphene transfer that follows. For midinfrared applications, silicon oxide (SiO_2) [72] and hexagonal boron nitride [73] have been popularly used as substrates for graphene, although plasmon losses due to strong plasmon-phonon coupling should be taken into consideration to determine the operation wavelength. Diamondlike carbon [59] and calcium fluoride (CaF_2) [74] can be good candidates, as they do not have polar phonons in this frequency range. The issue involving graphene and substrate losses is discussed in Appendix B. The insulating property and dielectric strength of the material used for the optical spacer becomes one of the important design parameters, from which the tunable range of graphene conductivity is largely determined. Another important aspect is addressing individual ribbons for separate doping. A recent work [75] demonstrated that having embedded local gating structures with graphene is experimentally feasible. The large dielectric thickness arising from the quarter-wavelength requirement could potentially impede electrical gating, as a voltage of about 700 V is required to achieve $E_F = 0.3$ eV, with a dielectric thickness of 3.93 μm and a static dielectric constant of 6.8 (for CaF_2). The dielectric breakdown limit of CaF_2 is 14.44 MV/cm [76], which, in this case, gives a breakdown voltage of approximately 5600 V. Despite being below the breakdown limit, such high values of gate voltages could be impractical from an experimental point of view. We could employ several strategies to make this electrical gating more experimentally favorable. We could decrease the operating wavelength and/or choose a spacer layer with a higher dielectric constant, which would decrease the thickness. Moreover, other techniques of doping graphene, such as chemical doping [77] and using ion gel [78], could also be explored.

ACKNOWLEDGMENTS

This work is supported by DARPA Grants No. FA86501627640 and No. HR00111710006, partially supported by NSF Grant No. DMS-1600578, and the University of Minnesota MRSEC under Grant No. DMR-1420013.

APPENDIX A: GENERALIZED SNELL'S LAW IN VECTOR FORM

Let rays of light be incident from point $S = (s_1, s_2, s_3)$, at a point $P(x_1, x_2, x_3 = a)$ on a plane, Γ, parallel to the x_1-x_2 plane, located at $x_3 = a$. Incident rays are then reflected to a point $D = (d_1, d_2, d_3)$. The normal to P is $\boldsymbol{\nu} = \hat{k} \equiv (0, 0, 1)$ (see Fig. 6). Therefore, the incident unit vector from S into a point P on Γ is $\boldsymbol{\alpha} = (\overrightarrow{SP}/|\overrightarrow{SP}|)$, and the reflected unit vector from P into D is $\boldsymbol{\beta} = (\overrightarrow{PD}/|\overrightarrow{PD}|)$. Since the ray is propagating in vacuum, from Fermat's principle, the least-optical paths for the incident and reflected rays are given by $|\overrightarrow{SP}|$ and $|\overrightarrow{DP}|$, and the corresponding accumulated phases are given by $k_0|\overrightarrow{SP}|$ and $k_0|\overrightarrow{DP}|$, respectively, where k_0 is the free-space wave number and $|\cdot|$ denotes the Euclidean distance. We introduce a phase discontinuity ϕ along Γ. According to the principle of stationary phase [6,79], we then seek to minimize the total phase $k_0|\overrightarrow{SP}| + k_0|\overrightarrow{DP}| - \phi(P)$ for $P \equiv (x_1, x_2, a)$ in Γ. Therefore, at the extreme point on Γ, by differentiating the total phase with respect to x_1 and x_2, we must have

$$k_0 \frac{x_1 - s_1}{|\overrightarrow{SP}|} + k_0 \frac{x_1 - d_1}{|\overrightarrow{DP}|} = \frac{\partial\phi}{\partial x_1},$$

$$k_0 \frac{x_2 - s_2}{|\overrightarrow{SP}|} + k_0 \frac{x_2 - d_2}{|\overrightarrow{DP}|} = \frac{\partial\phi}{\partial x_2},$$

which, from the definitions of $\boldsymbol{\alpha}$ and $\boldsymbol{\beta}$ above, can be rewritten as

$$(k_0\boldsymbol{\alpha} - k_0\boldsymbol{\beta}) \cdot \hat{i} = \frac{\partial\phi}{\partial x_1}, \qquad (k_0\boldsymbol{\alpha} - k_0\boldsymbol{\beta}) \cdot \hat{j} = \frac{\partial\phi}{\partial x_2}$$

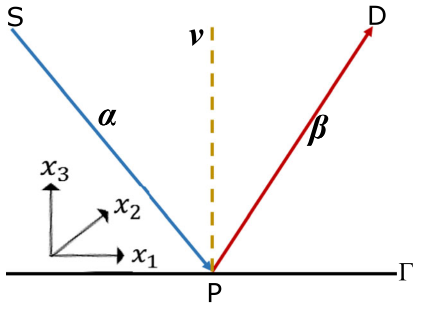

FIG. 6. Ray diagram illustrating the generalized Snell's law; see also Eq. (A1).

for x_1, x_2 and $x_3 = a$. Since the normal $\boldsymbol{\nu} = \hat{k}$, we therefore obtain the following expression of the generalized reflection law:

$$k_0\boldsymbol{\alpha} - k_0\boldsymbol{\beta} = \frac{\partial\phi}{\partial x_1}\hat{i} + \frac{\partial\phi}{\partial x_2}\hat{j} + \xi\boldsymbol{\nu}.$$

Notice that, when there is no phase discontinuity, i.e., $\phi = 0$, we recover the standard reflection law in vector form. If ϕ is defined in a small neighborhood of the plane Γ—i.e., $\phi(x_1, x_2, x_3)$ is defined for all x_1, x_2 quantities and for very small $x_3 - a$ values—then we can write the formula

$$\boldsymbol{\alpha} - \boldsymbol{\beta} = \frac{\boldsymbol{\nabla}\phi}{k_0} + \lambda\boldsymbol{\nu}, \tag{A1}$$

where λ is a scalar. Equation (A1) is the vector form of the generalized Snell's law for reflection.

APPENDIX B: THE EFFECT OF LOSS ON PHASE

The attainable range of reflection phase is dependent upon absorptive losses in the device. The reason for losing the phase shift of 2π with increased losses can be explained with arguments based on coupled-mode theory (CMT). The graphene-substrate-metal device structure creates an asymmetric Fabry-Perot resonator with a perfectly reflective mirror (metal) and a partially reflective mirror (graphene–dielectric layer interface). This can be effectively described as a one-port single resonator, working at a resonant frequency of ω_0 [80]. According to CMT, when the resonator is excited by an external excitation of frequency ω, the reflection coefficient is given by [81]

$$r = \frac{\gamma_r - \gamma_a - i(\omega - \omega_0)}{\gamma_r + \gamma_a + i(\omega - \omega_0)},$$

where $\gamma_r = 1/\tau_r$ is the rate of external or radiative losses and $\gamma_a = 1/\tau_a$ is the rate of internal of absorptive losses. Figure 7(a) shows the plot of r in a complex plane for different ω_0 values with a fixed ω value. As can be seen in the plot, when absorptive losses are smaller than radiative losses ($\gamma_r > \gamma_a$), r covers all four quadrants in the complex plane and the reflection phase covers the whole $-\pi$-to-π range. This situation is referred to as underdamped. But when absorptive loss surpasses radiative loss, i.e., $\gamma_r < \gamma_a$, the phase of r can no longer go from $-\pi$ to π and the system is referred to as overdamped.

In our device, by changing E_F, the plasmon resonance frequency is varied, as $\omega_0 \propto \sqrt{(E_F)}$. The radiative losses ($\gamma_r$) are constant, as they are dependent on the dimensions of the device. The absorptive losses (γ_a) are proportional to the inverse of the relaxation time, $1/\tau$, and the imaginary part of the refractive index of the dielectric cavity, k. Hence, when τ is decreased or k is increased, the system moves from underdamped to overdamped and the 2π phase shift range is lost. In Fig. 7(b), the reflection phase is plotted as a function of E_F for different relaxation times τ. The phase shift range becomes much smaller than 2π when τ is decreased below 0.1 ps. Similar behavior can be seen when k is increased above 0.15. Both τ and k are parameters related to the total absorptive loss in the device. Similar phase behavior was observed in Ref. [80] for metal-insulator-metal–based metasurfaces.

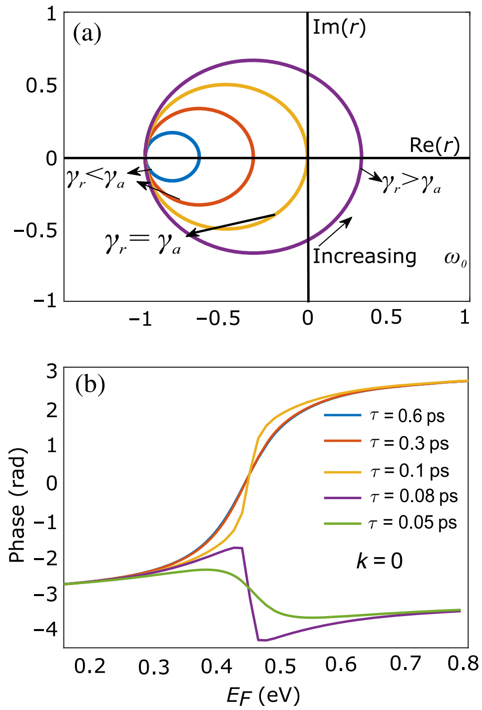

FIG. 7. Effect of intrinsic losses on the achievable phase range. (a) Complex plane plot of the reflection coefficient for the analytical model of the structure described in Ref. [81] using the single-port resonator model. When the intrinsic losses exceed the external or radiative losses, the phase of r cannot cover all four quadrants (the blue and red curves) of the complex plane, and the 2π phase shift is lost. (b) Simulation results of E_F vs the phase for the device with different relaxation times τ. As τ goes below 0.1 ps, we see a drastic change in phase profile.

APPENDIX C: COORDINATE REPRESENTATION OF THE VECTOR EQUATIONS FOR PHASE FUNCTION

The coordinate form of the vector equation (7) is

$$\frac{\partial\phi(P)}{\partial u_1} = k_0[\alpha_1 - \beta_1 + \delta g_{x_1}(X)],$$
$$\frac{\partial\phi(P)}{\partial u_2} = k_0[\alpha_2 - \beta_2 + \delta g_{x_2}(X)],$$
$$\frac{\partial\phi(P)}{\partial u_3} = k_0(\alpha_3 - \beta_3 - \delta).$$

The coordinate form of the vector equation (15) is

$$\frac{\partial\phi(P)}{\partial u_1} = 2k_0[\boldsymbol{\alpha}\cdot\boldsymbol{\eta}(P')]\left(\frac{-f_{x_1}(X)}{\sqrt{1+|\nabla f(X)|^2}} + [\boldsymbol{\eta}(P')\cdot\boldsymbol{\nu}(P)]\frac{g_{x_1}(X)}{\sqrt{1+|\nabla g(X)|^2}}\right),$$
$$\frac{\partial\phi(P)}{\partial u_2} = 2k_0[\boldsymbol{\alpha}\cdot\boldsymbol{\eta}(P')]\left(\frac{-f_{x_2}(X)}{\sqrt{1+|\nabla f(X)|^2}} + [\boldsymbol{\eta}(P')\cdot\boldsymbol{\nu}(P)]\frac{g_{x_2}(X)}{\sqrt{1+|\nabla g(X)|^2}}\right),$$
$$\frac{\partial\phi(P)}{\partial u_3} = 2k_0[\boldsymbol{\alpha}\cdot\boldsymbol{\eta}(P')]\left(\frac{1}{\sqrt{1+|\nabla f(X)|^2}} - [\boldsymbol{\eta}(P')\cdot\boldsymbol{\nu}(P)]\frac{1}{\sqrt{1+|\nabla g(X)|^2}}\right).$$

The coordinate form of the vector equation (19) is

$$\frac{\partial\phi(P)}{\partial u_1} = k_0\left\{\alpha_1 - \frac{d_1 - x_1}{|D-P|} + \left[\left(\boldsymbol{\alpha} - \frac{D-P}{|D-P|}\right)\cdot\boldsymbol{\nu}\right]\frac{g_{x_1}(X)}{\sqrt{1+|\nabla g(X)|^2}}\right\},$$
$$\frac{\partial\phi(P)}{\partial u_2} = k_0\left\{\alpha_2 - \frac{d_2 - x_2}{|D-P|} + \left[\left(\boldsymbol{\alpha} - \frac{D-P}{|D-P|}\right)\cdot\boldsymbol{\nu}\right]\frac{g_{x_2}(X)}{\sqrt{1+|\nabla g(X)|^2}}\right\},$$
$$\frac{\partial\phi(P)}{\partial u_3} = k_0\left\{\alpha_3 - \frac{d_3 - g(X)}{|D-P|} - \left[\left(\boldsymbol{\alpha} - \frac{D-P}{|D-P|}\right)\cdot\boldsymbol{\nu}\right]\frac{1}{\sqrt{1+|\nabla g(X)|^2}}\right\}.$$

APPENDIX D: INTEGRATING OF A SYSTEM OF DIFFERENTIAL EQUATIONS (16)

In this section, we integrate a system of differential equations, Eq. (16), obtained for the illusion optics case,

$$\frac{\partial\phi}{\partial x_1} = 2k_0[\boldsymbol{\alpha}\cdot\boldsymbol{\eta}(P')]\frac{g_{x_1}(X) - f_{x_1}(X)}{\sqrt{1+|\nabla f(X)|^2}} := A_1(X),$$
$$\frac{\partial\phi}{\partial x_2} = 2k_0[\boldsymbol{\alpha}\cdot\boldsymbol{\eta}(P')]\frac{g_{x_2}(X) - f_{x_2}(X)}{\sqrt{1+|\nabla f(X)|^2}} := A_2(X).$$

If ϕ and g are C^2, then the mixed partials $(\partial^2/\partial x_1\partial x_2)[\phi(X, g(X))]$ and $(\partial^2/\partial x_2\partial x_1)[\phi(X, g(X))]$ must be equal. Therefore, to have a solution ϕ, the following compatibility condition among $\boldsymbol{\alpha}$, f, and g must hold:

$$\frac{\partial}{\partial x_2}A_1(X) = \frac{\partial}{\partial x_1}A_2(X). \tag{D1}$$

In fact, if Eq. (D1) holds, we obtain the phase ϕ by integration as follows. To simplify the notation, set $h(X) = \phi(X, g(X))$. Thus, we need to solve the system

$$\frac{\partial h}{\partial x_1} = A_1, \qquad \frac{\partial h}{\partial x_2} = A_2.$$

Integrating the first equation with respect to x_1 yields

$$h(x_1, x_2) = \int_a^{x_1} A_1(s, x_2)ds + W(x_2).$$

Differentiating the last equation with respect to x_2 gives

$$\begin{aligned}\frac{\partial h}{\partial x_2}(x_1, x_2) &= \int_a^{x_1}\frac{\partial A_1}{\partial x_2}(s, x_2)ds + W'(x_2)\\ &= \int_a^{x_1}\frac{\partial A_2}{\partial x_1}(s, x_2)ds + W'(x_2) \quad [\text{from Eq.(D1)}]\\ &= A_2(x_1, x_2) - A_2(a, x_2) + W'(x_2).\end{aligned}$$

Thus, $W'(x_2) = A_2(a, x_2)$ and, by integration, $W(x_2) = \int_b^{x_2} A_2(a,t)dt + C$. Therefore, we obtain

$$\phi(X, g(X)) = \int_a^{x_1} A_1(s, x_2)ds + \int_b^{x_2} A_2(a,t)dt + C.$$

APPENDIX E: FOCUSING FROM POINT SOURCE TO POINT

Here, we devise a metasurface for reflective focusing due to a point source. Let $S(s_1, s_2, s_3)$ and $D(d_1, d_2, d_3)$ be two points above the surface parametrized by Eqs. (1) and (2). We seek a phase discontinuity so that all rays incident from S are reflected into D. Then the incident unit direction equals $(P - S)/|P - S|$ and the reflected unit direction equals $(D-P)/|D-P|$. From Eq. (4), we then seek ϕ so that

$$\frac{P-S}{|P-S|}-\frac{D-P}{|D-P|}-\frac{\boldsymbol{\nabla}\phi(P)}{k_0}=\lambda\boldsymbol{\nu}(P).$$

Following similar steps as discussed in Sec. V,

$$\frac{\boldsymbol{\nabla}\phi(P)}{k_0}=\frac{P-S}{|P-S|}-\frac{D-P}{|D-P|}-\left[\left(\frac{P-S}{|P-S|}-\frac{D-P}{|D-P|}\right)\cdot\boldsymbol{\nu}\right]\boldsymbol{\nu}.$$

Writing in coordinates yields

$$\begin{aligned}\phi_{u_1}&=k_0\left\{\frac{x_1-s_1}{|P-S|}-\frac{d_1-x_1}{|D-P|}\right.\\&\qquad\left.+\left[\left(\frac{P-S}{|P-S|}-\frac{D-P}{|D-P|}\right)\cdot\boldsymbol{\nu}\right]\frac{g_{x_1}(X)}{\sqrt{1+|\boldsymbol{\nabla}g(X)|^2}}\right\},\\\phi_{u_2}&=k_0\left\{\frac{x_2-s_2}{|P-S|}-\frac{d_2-x_2}{|D-P|}\right.\\&\qquad\left.+\left[\left(\frac{P-S}{|P-S|}-\frac{D-P}{|D-P|}\right)\cdot\boldsymbol{\nu}\right]\frac{g_{x_2}(X)}{\sqrt{1+|\boldsymbol{\nabla}g(X)|^2}}\right\},\\\phi_{u_3}&=k_0\left\{\frac{g(X)-s_3}{|P-S|}-\frac{d_3-g(X)}{|D-P|}\right.\\&\qquad\left.-\left[\left(\frac{P-S}{|P-S|}-\frac{D-P}{|D-P|}\right)\cdot\boldsymbol{\nu}\right]\frac{1}{\sqrt{1+|\boldsymbol{\nabla}g(X)|^2}}\right\}.\end{aligned}$$

Hence, by the chain rule,

$$\begin{aligned}\frac{\partial\phi}{\partial x_i}&=\frac{\partial\phi(u_1,u_2,u_3)}{\partial u_i}+\frac{\partial\phi(u_1,u_2,u_3)}{\partial u_3}\frac{\partial u_3}{\partial x_i}\\&=k_0\left(\frac{x_i-s_i}{|P-S|}-\frac{d_i-x_i}{|D-P|}\right.\\&\qquad\left.+\frac{g(X)-s_3}{|X-A|}g_{x_i}(X)-\frac{d_3-g(X)}{|D-P|}g_{x_i}(X)\right)\\&=k_0\left(\frac{\partial}{\partial x_i}|P-S|+\frac{\partial}{\partial x_i}|D-P|\right),\end{aligned}$$

with $i=1$ and 2. Therefore, we obtain the phase as

$$\phi=k_0(|P-S|+|D-P|)+C.$$

For a 2D geometry independent of x_2, $S=(x_s,z_s)$, and $D=(x_d,z_d)$, the phase equation reduces to

$$\begin{aligned}\phi(x_1)=k_0\Big(&\sqrt{(x_1-x_s)^2+[g(x_1)-z_s]^2}\\&+\sqrt{(x_1-x_d)^2+[g(x_1)-z_d]^2}\Big)+C.\end{aligned}\tag{E1}$$

[1] C. L. Holloway, E. F. Kuester, J. A. Gordon, J. O'Hara, J. Booth, and D. R. Smith, An overview of the theory and applications of metasurfaces: The two-dimensional equivalents of metamaterials, IEEE Antennas Propag. Mag. **54**, 10 (2012).

[2] N. Yu and F. Capasso, Flat optics with designer metasurfaces, Nat. Mater. **13**, 139 (2014).

[3] J. Scheuer, Metasurfaces-based holography and beam shaping: Engineering the phase profile of light, Nanophotonics **6**, 137 (2017).

[4] A. V. Kildishev, A. Boltasseva, and V. M. Shalaev, Planar photonics with metasurfaces, Science **339**, 1232009 (2013).

[5] N. Meinzer, W. L. Barnes, and I. R. Hooper, Plasmonic meta-atoms and metasurfaces, Nat. Photonics **8**, 889 (2014).

[6] N. Yu, P. Genevet, M. A. Kats, F. Aieta, J.-P. Tetienne, F. Capasso, and Z. Gaburro, Light propagation with phase discontinuities: Generalized laws of reflection and refraction, Science **334**, 333 (2011).

[7] F. Aieta, P. Genevet, M. A. Kats, N. Yu, R. Blanchard, Z. Gaburro, and F. Capasso, Aberration-free ultrathin flat lenses and axicons at telecom wavelengths based on plasmonic metasurfaces, Nano Lett. **12**, 4932 (2012).

[8] X. Ni, N. K. Emani, A. V. Kildishev, A. Boltasseva, and V. M. Shalaev, Broadband light bending with plasmonic nanoantennas, Science **335**, 427 (2012).

[9] S. Sun, K.-Y. Yang, C.-M. Wang, T.-K. Juan, W. T. Chen, C. Y. Liao, Q. He, S. Xiao, W.-T. Kung, G.-Y. Guo, L. Zhou, and D. P. Tsai, High-efficiency broadband anomalous reflection by gradient meta-surfaces, Nano Lett. **12**, 6223 (2012).

[10] Z. Li, E. Palacios, S. Butun, and K. Aydin, Visible-frequency metasurfaces for broadband anomalous reflection and high-efficiency spectrum splitting, Nano Lett. **15**, 1615 (2015).

[11] A. Nemilentsau and T. Low, Broadband achromatic anomalous mirror in near-IR and visible frequency ranges, ACS Photonics **4**, 1646 (2017).

[12] M. Farmahini-Farahani and H. Mosallaei, Birefringent reflectarray metasurface for beam engineering in infrared, Opt. Lett. **38**, 462 (2013).

[13] C. Pfeiffer and A. Grbic, Cascaded metasurfaces for complete phase and polarization control, Appl. Phys. Lett. **102**, 231116 (2013).

[14] A. Pors, O. Albrektsen, I. P. Radko, and S. I. Bozhevolnyi, Gap plasmon-based metasurfaces for total control of reflected light, Sci. Rep. **3**, 2155 (2013).

[15] X. Yin, Z. Ye, J. Rho, Y. Wang, and X. Zhang, Photonic spin Hall effect at metasurfaces, Science **339**, 1405 (2013).

[16] C. Wu, N. Arju, G. Kelp, J. A. Fan, J. Dominguez, E. Gonzales, E. Tutuc, I. Brener, and G. Shvets, Spectrally selective chiral silicon metasurfaces based on infrared Fano resonances, Nat. Commun. **5**, 3892 (2014).

[17] A. Arbabi, Y. Horie, M. Bagheri, and A. Faraon, Dielectric metasurfaces for complete control of phase and polarization with subwavelength spatial resolution and high transmission, Nat. Nanotechnol. **10**, 937 (2015).

[18] A. Shaltout, J. Liu, A. Kildishev, and V. Shalaev, Photonic spin Hall effect in gap-plasmon metasurfaces for on-chip chiroptical spectroscopy, Optica **2**, 860 (2015).

[19] N. Yu, F. Aieta, P. Genevet, M. A. Kats, Z. Gaburro, and F. Capasso, A broadband, background-free quarter-wave plate based on plasmonic metasurfaces, Nano Lett. **12**, 6328 (2012).

[20] Y. Zhao and A. Alù, Tailoring the dispersion of plasmonic nanorods to realize broadband optical meta-waveplates, Nano Lett. **13**, 1086 (2013).

[21] F. Ding, Z. Wang, S. He, V. M. Shalaev, and A. V. Kildishev, Broadband high-efficiency half-wave plate: A supercell-based plasmonic metasurface approach, ACS Nano **9**, 4111 (2015).

[22] B. Memarzadeh and H. Mosallaei, Array of planar plasmonic scatterers functioning as light concentrator, Opt. Lett. **36**, 2569 (2011).

[23] X. Chen, L. Huang, H. Mühlenbernd, G. Li, B. Bai, Q. Tan, G. Jin, C.-W. Qiu, S. Zhang, and T. Zentgraf, Dual-polarity plasmonic metalens for visible light, Nat. Commun. **3**, 1198 (2012).

[24] F. Monticone, N. M. Estakhri, and A. Alù, Full Control of Nanoscale Optical Transmission with a Composite Metascreen, Phys. Rev. Lett. **110**, 203903 (2013).

[25] X. Ni, S. Ishii, A. V. Kildishev, and V. M. Shalaev, Ultra-thin, planar, Babinet-inverted plasmonic metalenses, Light Sci. Appl. **2**, e72 (2013).

[26] X. Li, S. Xiao, B. Cai, Q. He, T. J. Cui, and L. Zhou, Flat metasurfaces to focus electromagnetic waves in reflection geometry, Opt. Lett. **37**, 4940 (2012).

[27] A. Pors, M. G. Nielsen, R. L. Eriksen, and S. I. Bozhevolnyi, Broadband focusing flat mirrors based on plasmonic gradient metasurfaces, Nano Lett. **13**, 829 (2013).

[28] M. Veysi, C. Guclu, O. Boyraz, and F. Capolino, Thin anisotropic metasurfaces for simultaneous light focusing and polarization manipulation, J. Opt. Soc. Am. B **32**, 318 (2015).

[29] W. Ma, D. Jia, X. Yu, Y. Feng, and Y. Zhao, Reflective gradient metasurfaces for polarization-independent light focusing at normal or oblique incidence, Appl. Phys. Lett. **108**, 071111 (2016).

[30] S. Zhang, M.-H. Kim, F. Aieta, A. She, T. Mansuripur, I. Gabay, M. Khorasaninejad, D. Rousso, X. Wang, M. Troccoli, N. Yu, and F. Capasso, High efficiency near diffraction-limited mid-infrared flat lenses based on metasurface reflectarrays, Opt. Express **24**, 18024 (2016).

[31] Q. Fan, P. Huo, D. Wang, Y. Liang, F. Yan, and T. Xu, Visible light focusing flat lenses based on hybrid dielectric-metal metasurface reflector-arrays, Sci. Rep. **7**, 45044 (2017).

[32] J. Li and J. B. Pendry, Hiding under the Carpet: A New Strategy for Cloaking, Phys. Rev. Lett. **101**, 203901 (2008).

[33] Y. Lai, J. Ng, H. Y. Chen, D. Z. Han, J. J. Xiao, Z.-Q. Zhang, and C. T. Chan, Illusion Optics: The Optical Transformation of an Object into Another Object, Phys. Rev. Lett. **102**, 253902 (2009).

[34] R. Fleury and A. Alù, Cloaking and invisibility: A review, Forum Electromagn. Res. Methods Appl. Technol. **1**, 9 (2014).

[35] N. M. Estakhri and A. Alù, Ultra-thin unidirectional carpet cloak and wavefront reconstruction with graded metasurfaces, IEEE Antennas Wireless Propag. Lett. **13**, 1775 (2014).

[36] N. M. Estakhri, C. Argyropoulos, and A. Alù, Graded metascreens to enable a new degree of nanoscale light management, Phil. Trans. R. Soc. A **373**, 20140351 (2015).

[37] B. Orazbayev, N. M. Estakhri, M. Beruete, and A. Alù, Terahertz carpet cloak based on a ring resonator metasurface, Phys. Rev. B **91**, 195444 (2015).

[38] Y. Yang, H. Wang, F. Yu, Z. Xu, and H. Chen, A metasurface carpet cloak for electromagnetic, acoustic and water waves, Sci. Rep. **6**, 20219 (2016).

[39] H. Tao, Z. Yang, Z. Wang, and M. Zhao, Polarization-independent metasurface cloak for visible light, J. Opt. Soc. Am. B **33**, 2251 (2016).

[40] J. Cheng, S. Jafar-Zanjani, and H. Mosallaei, All-dielectric ultrathin conformal metasurfaces: Lensing and cloaking applications at 532 nm wavelength, Sci. Rep. **6**, 38440 (2016).

[41] Y. Yang, L. Jing, B. Zheng, R. Hao, W. Yin, E. Li, C. M. Soukoulis, and H. Chen, Full-polarization 3D metasurface cloak with preserved amplitude and phase, Adv. Mater. **28**, 6866 (2016).

[42] Y.-W. Huang, H. W. H. Lee, R. Sokhoyan, R. A. Pala, K. Thyagarajan, S. Han, D. P. Tsai, and H. A. Atwater, Gate-tunable conducting oxide metasurfaces, Nano Lett. **16**, 5319 (2016).

[43] J. Sautter, I. Staude, M. Decker, E. Rusak, D. N. Neshev, I. Brener, and Y. S. Kivshar, Active tuning of all-dielectric metasurfaces, ACS Nano **9**, 4308 (2015).

[44] S. M. Kamali, E. Arbabi, A. Arbabi, Y. Horie, and A. Faraon, Highly tunable elastic dielectric metasurface lenses, Laser Photonics Rev. **10**, 1002 (2016).

[45] T. Low and P. Avouris, Graphene plasmonics for terahertz to mid-infrared applications, ACS Nano **8**, 1086 (2014).

[46] A. Grigorenko, M. Polini, and K. Novoselov, Graphene plasmonics, Nat. Photonics **6**, 749 (2012).

[47] F. J. Garcia de Abajo, Graphene plasmonics: Challenges and opportunities, ACS Photonics **1**, 135 (2014).

[48] Y. V. Bludov, A. Ferreira, N. Peres, and M. Vasilevskiy, A primer on surface plasmon-polaritons in graphene, Int. J. Mod. Phys. B **27**, 1341001 (2013).

[49] L. Malard, M. Pimenta, G. Dresselhaus, and M. Dresselhaus, Raman spectroscopy in graphene, Phys. Rep. **473**, 51 (2009).

[50] P. Avouris, T. F. Heinz, and T. Low, *2D Materials* (Cambridge University Press, Cambridge, England, 2017).

[51] J. Christensen, A. Manjavacas, S. Thongrattanasiri, F. H. Koppens, and F. J. Garcia de Abajo, Graphene plasmon waveguiding and hybridization in individual and paired nanoribbons, ACS Nano **6**, 431 (2012).

[52] A. Fallahi and J. Perruisseau-Carrier, Design of tunable biperiodic graphene metasurfaces, Phys. Rev. B **86**, 195408 (2012).

[53] E. Carrasco, M. Tamagnone, and J. Perruisseau-Carrier, Tunable graphene reflective cells for thz reflectarrays and generalized law of reflection, Appl. Phys. Lett. **102**, 104103 (2013).

[54] E. Carrasco, M. Tamagnone, J. R. Mosig, T. Low, and J. Perruisseau-Carrier, Gate-controlled mid-infrared light bending with aperiodic graphene nanoribbons array, Nanotechnology **26**, 134002 (2015).

[55] M. C. Sherrott, P. W. Hon, K. T. Fountaine, J. C. Garcia, S. M. Ponti, V. W. Brar, L. A. Sweatlock, and H. A. Atwater, Experimental demonstration of >230 phase modulation in gate-tunable graphene-gold reconfigurable mid-infrared metasurfaces, Nano Lett. **17**, 3027 (2017).

[56] R. Yu, V. Pruneri, and F. J. Garcia de Abajo, Resonant visible light modulation with graphene, ACS Photonics **2**, 550 (2015).

[57] P. Chen, M. Farhat, A. N. Askarpour, M. Tymchenko, and A. Alù, Infrared beam-steering using acoustically modulated surface plasmons over a graphene monolayer, J. Opt. **16**, 094008 (2014).

[58] T. Yatooshi, A. Ishikawa, and K. Tsuruta, Terahertz wavefront control by tunable metasurface made of graphene ribbons, Appl. Phys. Lett. **107**, 053105 (2015).

[59] H. Yan, T. Low, W. Zhu, Y. Wu, M. Freitag, X. Li, F. Guinea, P. Avouris, and F. Xia, Damping pathways of mid-infrared plasmons in graphene nanostructures, Nat. Photonics **7**, 394 (2013).

[60] L. Ju, B. Geng, J. Horng, C. Girit, M. Martin, Z. Hao, H. A. Bechtel, X. Liang, A. Zettl, Y. R. Shen, and F. Wang, Graphene plasmonics for tunable terahertz metamaterials, Nat. Nanotechnol. **6**, 630 (2011).

[61] X. Ni, Z. J. Wong, M. Mrejen, Y. Wang, and X. Zhang, An ultrathin invisibility skin cloak for visible light, Science **349**, 1310 (2015).

[62] P.-Y. Chen and A. Alù, Mantle cloaking using thin patterned metasurfaces, Phys. Rev. B **84**, 205110 (2011).

[63] Y. Lai, J. Ng, H. Y. Chen, D. Z. Han, J. J. Xiao, Z.-Q. Zhang, and C. T. Chan, Illusion Optics: The Optical Transformation of an Object into Another Object, Phys. Rev. Lett. **102**, 253902 (2009).

[64] R. K. Luneburg and M. Herzberger, *Mathematical Theory of Optics* (University of California Press, Berkeley, 1964).

[65] C. E. Gutiérrez, L. Pallucchini, and E. Stachura, General refraction problems with phase discontinuities on nonflat metasurfaces, J. Opt. Soc. Am. A **34**, 1160 (2017).

[66] COMSOL and Inc., COMSOL MULTIPHYSICS, version 5.2, 2015.

[67] M. Wei, Q. Yang, X. Zhang, Y. Li, J. Gu, J. Han, and W. Zhang, Ultrathin metasurface-based carpet cloak for terahertz wave, Opt. Express **25**, 15635 (2017).

[68] Y. Lee, S. Bae, H. Jang, S. Jang, S.-E. Zhu, S. H. Sim, Y. I. Song, B. H. Hong, and J.-H. Ahn, Wafer-scale synthesis and transfer of graphene films, Nano Lett. **10**, 490 (2010).

[69] L. G. Martins, Y. Song, T. Zeng, M. S. Dresselhaus, J. Kong, and P. T. Araujo, Direct transfer of graphene onto flexible substrates, Proc. Natl. Acad. Sci. U.S.A. **110**, 17762 (2013).

[70] Y. Wang, R. Yang, Z. Shi, L. Zhang, D. Shi, E. Wang, and G. Zhang, Super-elastic graphene ripples for flexible strain sensors, ACS Nano **5**, 3645 (2011).

[71] M. Hofmann, Y.-P. Hsieh, A. L. Hsu, and J. Kong, Scalable, flexible and high resolution patterning of CVD graphene, Nanoscale **6**, 289 (2014).

[72] D. Rodrigo, O. Limaj, D. Janner, D. Etezadi, F. J. G. de Abajo, V. Pruneri, and H. Altug, Mid-infrared plasmonic biosensing with graphene, Science **349**, 165 (2015).

[73] S. Dai, Q. Ma, M. Liu, T. Andersen, Z. Fei, M. Goldflam, M. Wagner, K. Watanabe, T. Taniguchi, M. Thiemens, F. Keilmann, G. C. A. M. Janssen, S.-E. Zhu, P. Jarillo-Herrero, M. M. Fogler, and D. N. Basov, Graphene on hexagonal boron nitride as a tunable hyperbolic metamaterial, Nat. Nanotechnol. **10**, 682 (2015).

[74] H. Hu, X. Yang, F. Zhai, D. Hu, R. Liu, K. Liu, Z. Sun, and Q. Dai, Far-field nanoscale infrared spectroscopy of vibrational fingerprints of molecules with graphene plasmons, Nat. Commun. **7**, 12334 (2016).

[75] A. Barik, Y. Zhang, R. Grassi, B. P. Nadappuram, J. B. Edel, T. Low, S. J. Koester, and S.-H. Oh, Graphene-edge dielectrophoretic tweezers for trapping of biomolecules, Nat. Commun. **8**, 1867 (2017).

[76] W. L. Smith, J. Bechtel, and N. Bloembergen, Dielectric-breakdown threshold and nonlinear-refractive-index measurements with picosecond laser pulses, Phys. Rev. B **12**, 706 (1975).

[77] H. Liu, Y. Liu, and D. Zhu, Chemical doping of graphene, J. Mater. Chem. **21**, 3335 (2011).

[78] Z. Miao, Q. Wu, X. Li, Q. He, K. Ding, Z. An, Y. Zhang, and L. Zhou, Widely Tunable Terahertz Phase Modulation with Gate-Controlled Graphene Metasurfaces, Phys. Rev. X **5**, 041027 (2015).

[79] F. Aieta, P. Genevet, N. Yu, M. A. Kats, Z. Gaburro, and F. Capasso, Out-of-plane reflection and refraction of light by anisotropic optical antenna metasurfaces with phase discontinuities, Nano Lett. **12**, 1702 (2012).

[80] C. Qu, S. Ma, J. Hao, M. Qiu, X. Li, S. Xiao, Z. Miao, N. Dai, Q. He, S. Sun, and L. Zhou, Tailor the Functionalities of Metasurfaces Based on a Complete Phase Diagram, Phys. Rev. Lett. **115**, 235503 (2015).

[81] H. A. Haus, *Waves and Fields in Optoelectronics* (Prentice-Hall, Englewood Cliffs, NJ, 1984).